MHD SIMULATION OF COMETS: THE PLASMA ENVIRONMENT OF COMET HALE–BOPP

TAMAS I. GOMBOSI, KENNETH C. HANSEN, DARREN L. DeZEEUW and MICHAEL R. COMBI
Space Physics Research Laboratory, Department of Atmospheric Oceanic and Space Sciences, The University of Michigan, Ann Arbor, MI 48109, USA

KENNETH G. POWELL
W.M. Keck Foundation CFD Laboratory, Department of Aerospace Engineering, The University of Michigan, Ann Arbor, MI 48109, USA

(Received 21 February 1998; Accepted 31 August 1998)

Abstract. MHD simulation results of the interaction of the expanding atmosphere of comet Hale–Bopp with the magnetized solar wind are presented. At the upstream boundary a supersonic and superalfvénic solar wind enters into the simulation box 25 million km upstream of the nucleus. The solar wind is continuously mass loaded with cometary ions originating from the nucleus. The effects of photoionization, recombination and ion-neutral frictional drag are taken into account in the model. The governing equations are solved on an adaptively refined unstructured Cartesian grid using our MUSCL-type upwind numerical technique, MAUS-MHD (Multiscale Adaptive Upwind Scheme for MHD). The combination of the adaptive refinement with the MUSCL-scheme allows the entire cometary atmosphere to be modeled, while still resolving both the shock and the diamagnetic cavity of the comet.

Detailed simulation results for the plasma environment of comet Hale–Bopp for slow and fast solar wind conditions are presented. We also calculate synthetic H_2O^+, CO^+ and soft x–ray images for observing conditions on April 11, 1997.

Keywords: MHD, comets, Hale–Bopp, cometary x-rays

Abbreviations: MHD – Magnetohydrodynamics

1. Introduction

Our present understanding of cometary atmospheres is based on Whipple's "dirty iceball" idea in which the nucleus consists of a mixture of frozen volatiles and non-volatile dust (Whipple, 1950). As cometary nuclei approach the sun, water vapor and other volatile gases sublimate from the surface layers generating a rapidly expanding cloud of dust and gas. Along with the various gas species, particles of the less volatile material (mainly refractory silicates and organic CHON grains) are released in the sublimation process and are subsequently dragged along by the gas, eventually forming a dust coma and tail.

Earth, Moon and Planets **79:** 179–207, 1997.

The sublimated gas molecules and atoms undergo collisions and various fast photochemical processes, thus producing a whole series of daughter molecules and ions which form the cometary ionosphere. Most of the species observed in comets are chemically unstable radicals which are clearly photo-destruction products of more stable parent molecules which are sublimated from the nucleus and possibly from a halo of volatile grains. It has also been suggested that heterogeneous chemistry involving neutral molecules, ions and charged dust grains might play a role in coma aeronomy.

A well developed cometary atmosphere extends to distances several orders of magnitude larger than the size of the nucleus. It is the mass loading of the solar wind with newly created cometary ions, from this extended exosphere, that is responsible for the interaction with the solar wind. Mass loading occurs when a magnetized plasma moves through a background of neutral particles which is continuously ionized. Photoionization and electron impact ionization result in the addition of plasma to the plasma flow, while charge exchange replaces fast ions with almost stationary ones. "Ion pickup" (or ion implantation) is the process of accommodation (but not thermalization) of a single newborn ion to the plasma flow. The combined effect of the various ionization processes is usually net mass addition. Conservation of momentum and energy requires that the plasma flow be decelerated as newly born charged particles are "picked up". The process of continuous ion pickup and its feedback to the plasma flow is called "mass loading".

For recent summaries of our present understanding of comets we refer to the excellent review by Festou et al. (1993a,b). Several monographs also offer detailed discussions (cf. Huebner, 1990; Newburn et al., 1991; Gombosi, 1993).

2. Coma Chemistry and Energetics

Most of the species observed in cometary atmospheres are chemically unstable radicals, which clearly are photo-destruction products of more stable parent molecules. Chemical reactions between evaporated parent molecules are very slow and of secondary importance, while dissociation and ionization by solar UV radiation produce highly reactive radicals and ions.

Unlike the ion chemistry in the coma which is sparked by photochemistry (but where the detailed composition is controlled by fast ion-neutral reactions) the neutral chemistry is controlled in large measure by photochemistry. As comets approach the sun on their typically eccentric orbits, the vaporization of the coma becomes far more active for distances from the sun <2.5 AU. The best estimate for the composition of the gaseous component of a "typical" comet is 80% water, about 5% each of CH_3OH, and other organics, 3% CO_2, 0.5% NH_3 and <1% HCN, CH_3CH, C_2H_2, etc. (A'Hearn and Festou, 1990). There is significant CO and H_2CO in comets (up to 10–20% total CO in some comets).

It should be expected that the neutral composition of the very inner coma will be dominated by the primary parent molecules emitted directly from the nucleus, the molecules emitted by an extended source of volatile grains, and a combination of the principal dissociation products of the major species (H, OH, CO) which are produced slowly, as well as the fast photodissociation products of more minor species (e.g., NH_2). Photodissociative ionization (such as $CO_2 + h\nu \rightarrow O + CO^+ + e + 27.1$ eV) is one of the most important processes of cometary aeronomy. The excess electron energy is typically several tens of eV. This process is probably most important deep in the coma. Another very important reaction is electron-dissociative recombination (an example is $O_2^+ + e \rightarrow O(^1D) + O(^1P) + 4.98$eV). The products often have relatively high kinetic energies and/or are in an excited state. Because of the Coulomb interaction between electrons and ions, this process has a very large cross section.

One of the major surprises from the Giotto measurements at comet Halley was the detection of an ion density peak at about 10^4 km from the nucleus (Balsiger et al., 1986). Theoretical suggestions that this peak could be caused by a rapid, two orders of magnitude change in the electron temperature (Körösmezey et al., 1987; Ip et al., 1987) have recently been confirmed by a detailed analysis of the Giotto mass spectrometer data (Altwegg et al., 1993; Eberhardt and Krankowsky, 1995). Inside the collision dominated region the electron temperature is almost equal to the neutral temperature ($\sim$100 K), due to strong cooling by rotational and vibrational excitation of water molecules. Outside the collisional region the H_2O radiative cooling rapidly becomes negligible and photoelectron heating and solar wind heat flux determine the electron temperature. The transition between the two regions is quite rapid, resulting in the observed rapid rise of the electron temperature and the related ion density (recombination rapidly decreases with increasing electron temperature).

The most abundant molecules in comet Halley's coma were H_2O ($\sim$80%), CO and CO_2. Also, higher abundances of complex carbon hydroxites were found than anticipated (Altwegg et al., 1993). The main photoionization product in the cometary coma is H_2O^+. These water ions transfer a proton to other neutral molecules which have higher proton affinity than the OH radical (the prime example is $H_2O^+ + H_2O \rightarrow H_3O^+ + OH$). The proton affinity of the parent molecules determines the reaction rate, therefore protonated ions of molecules with high proton affinity are more abundant (relative to other ions) than their parent molecules are (Altwegg et al., 1994).

3. Solar Wind Interaction

Neutral atoms and molecules of cometary origin move along ballistic trajectories (with velocities ranging from $\sim$0.5 km s^{-1} to a few tens of km s^{-1}) and become

ionized with a characteristic ionization lifetime of 10^5–10^7 s (cf. Gombosi et al., 1986).

Freshly born ions are accelerated by the motional electric field of the high-speed solar wind flow. The ion trajectory is cycloidal, resulting from the superposition of gyration and E×B drift. The corresponding velocity-space distribution is a ring-beam distribution, where the gyration speed of the ring is $u \sin\alpha$, (where u is the bulk plasma speed and α is the angle between the solar wind velocity and magnetic field vectors) and the beam velocity (along the magnetic field line) is $u \cos\alpha$. The ring beam distribution has large velocity space gradients and it is unstable to the generation of low frequency transverse waves.

The combination of ambient and self-generated magnetic field turbulence pitch-angle scatters the newborn ions from the pickup ring. In a first approximation the pickup particles interact with the low frequency waves without significantly changing their energy in the average wave frame. As a result of this process the pitch angles of the pickup-ring particles are scattered on the spherical velocity space shell of radius u around the local solar wind velocity (cf. Neugebauer, 1990; Motschmann and Glassmeier, 1993; Coates et al., 1993).

Implanted ions were detected at comets Giacobini-Zinner, Halley, and Grigg-Skjellerup as large fluxes of energetic particles (Coates et al., 1993; Hynds et al., 1986; McKenna-Lawlor et al., 1986; Somogyi et al., 1986). A significant part of the detected energetic ion population was observed at energies considerably larger than the pickup energy, indicating the presence of some kind of acceleration process acting on implanted ions. The primary acceleration mechanism turned out to be slow velocity diffusion of lower energy implanted ions (Coates et al., 1989; Gombosi et al., 1991; Neugebauer et al., 1989).

Conservation of momentum and energy require that the solar wind be decelerated as newly born charged particles are "picked up" by the plasma flow. Continuous deceleration of the solar wind flow by mass loading is possible only up to a certain point at which the mean molecular weight of the plasma particles reaches a critical value. At this point a weak shock forms and impulsively decelerates the flow to subsonic velocities. Bow shock crossings were identified in the data from each of the Halley flyby spacecraft at approximately the expected locations. The shock jumps were clearly defined in many of the observations from the plasma probes and magnetometers on Giotto, VEGA and Suisei. For Giacobini-Zinner and Grigg-Skjellerup it is generally recognized that the pickup ions generated so much mass loading and turbulence that the shock crossing was extremely thick. The cometary "shock wave" is quite different than the "classical" planetary and interplanetary shocks, because the deceleration and dissipation is due to mass loading and wave-particle interaction which take place over a very large region with the "shock" being only the downstream boundary of an extended distributed process (cf. Ip and Axford, 1990).

The cometosheath is located between the cometary shock and the magnetic field free region in the innermost coma. The plasma population in the cometosheath is

a changing mixture of ambient solar wind and particles picked up upstream and downstream of the shock. The distinction between cometary particles picked up outside and inside the shock is important because of the large difference in their random energy. The random energy of ions in a pickup shell is typically 20 keV for water group ions picked up upstream of the shock. Cometary ions born behind the shock are picked up at smaller velocities, and consequently, the random energy of their pickup shell is significantly smaller than that of ions born upstream of the shock. Overall, ions retain (in their energy) a memory of where they were born, and the plasma frame energy of pickup ions decreases with decreasing cometocentric distance. The observed distribution functions are complicated (cf. Nagai et al., 1984; Neugebauer, 1990).

One of the debated issues is whether or not energetic electrons are a permanent feature of the cometosheath. The electron spectrometer on Giotto observed large fluxes of energetic (0.8–3.6 keV) electrons in the so called "mystery region" between about 8.5×10^3 and 5.5×10^3 km (Réme, 1991). At a cometocentric distance of about 5.5×10^3 km these fluxes abruptly disappeared, simultaneously with a sudden decrease of the total ion density and velocity and an increase of the ion temperature. At the same time the magnetic field changed direction and became much smoother. Réme (1991) interpreted this change as a permanent feature of the cometosheath and found similar events in the Vega and Suisei data sets. A different view was presented by Gringauz and Verigin (1991), who did not see evidence of the presence of energetic electrons in the cometosheath and interpret the Giotto energetic electron event as a transient feature generated by a passing interplanetary disturbance.

Another very interesting feature in the cometosheath is the cometopause, discovered by the Vega plasma instrument (Gringauz et al., 1986). At around 1.65×10^5 km the PLASMAG instrument observed a sharp transition from a primarily solar wind proton dominated plasma population to a mainly cometary water group ion plasma. This transition was also accompanied by a moderate increase in the low frequency plasma wave intensity, while there were no obvious changes in the magnetic field. The unexpected feature of the cometopause was not its existence, but its sharpness. Gombosi (1987) suggested that an "avalanche" of charge exchange collisions in the decelerating plasma flow can rapidly deplete the solar wind proton population and replace it with slower water group ions.

Inside the cometopause ion-neutral chemistry and recombination starts to become more and more important. In the inner coma an "ionopause" or "dimagnetic cavity boundary", separates the solar wind controlled magnetized plasma from the magnetic field free, cometary ionosphere. At a cometocentric distance of about 4600 km the Giotto magnetometer detected a very sharp drop of the magnetic field magnitude from about 60 nT to practically zero (Neubauer et al., 1986). Behind this boundary the spacecraft entered into a magnetic field free region, the diamagnetic cavity. The inner edge of the diamagnetic cavity boundary was very thin: the field decresed from 20 nT to zero within about 25 km (Neubauer, 1988). It has been

recognized shortly after the Giotto encounter that the dominant factor leading to the formation of diamagnetic cavity boundary is the balance between the outward ion-neutral frictional force and the inward pointing J×B force (which is a combination of the magnetic pressure gradient and the curvature forces) (Cravens, 1986; Ip et al., 1987).

Deep inside the diamagnetic cavity the cometary plasma and the neutral gas are very strongly coupled by ion-neutral collisions, and they move radially outward with the same expansion velocity. Outside the cavity the plasma is nearly stagnated. It was predicted that an inner shock might be formed well inside the ionopause (Wallis and Dryer, 1976). This inner shock was assumed to decelerate the supersonic cometary ion outflow to subsonic velocities and divert the flow towards the plasma tail. Most of the plasma entering the transition layer from the diamagnetic cavity is consumed by recombination inside the boundary layer, which separates the cometary plasma flow from the stagnated solar wind controlled outside flow (Cravens, 1989; Damas and Mendis, 1992). This means that the inner shock is very close to the diamagnetic cavity boundary, and there is a thin density spike between the shock and the diamagnetic cavity boundary. A very high resolution analysis of the Giotto ion mass spectrometer data confirmed the existence of the density enhancement (Goldstein et al., 1989).

4. Solar Wind Stream Structure

Near the ecliptic plane the solar wind tends to be organized into alternating slow and fast streams. In fast streams the solar wind speed typically exceeds 600 km s^{-1}, while in slow streams the speed is usually less than 350 km s^{-1}. These streams tend to be encountered by Earth on several successive solar rotations. High-speed streams are typically unipolar.

The long-lived high-speed streams originate in coronal holes, which are large, nearly unipolar regions in the solar atmosphere. Since these regions are associated with open magnetic field lines the solar wind expansion is relatively unrestricted by the solar magnetic field. Low speed flows, on the other hand, originate in the outer regions of coronal streamers that straddle regions of magnetic polarity reversals. It is very likely that low speed solar wind flows are related to complicated open magnetic field line topologies in the coronal streamer belt.

The solar magnetic field undergoes significant changes during the solar cycle. Near solar minimum (including the declining phase of the solar cycle) large, long-lived coronal holes extend from the polar regions to low heliographic latitudes. High-speed solar wind streams originating from these coronal holes are quite commonly observed near the ecliptic plane during this phase of the solar cycle. Figure 1 illustrates the variable solar wind at low heliolatitudes and the persistent high-speed flows at high latitudes during the declining phase of the solar cycle and near solar minimum. It shows the solar wind speed as a function of heliospheric latitude

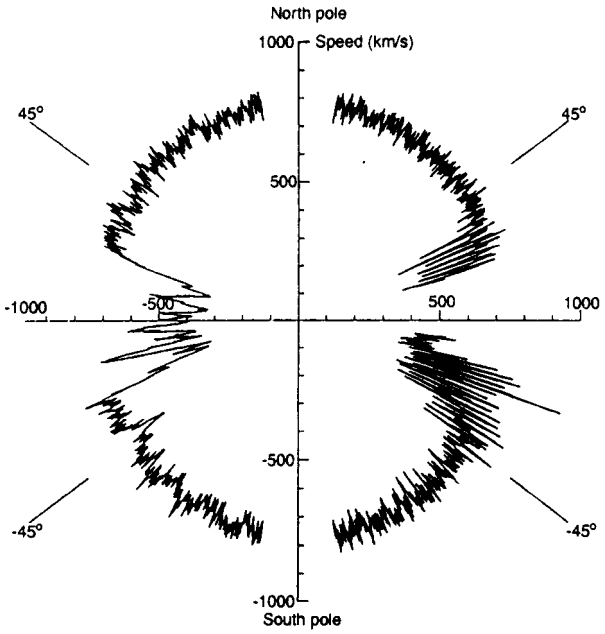

Figure 1. Solar wind speed as a function of heliographic latitude as measured by the Ulysses spacecraft in 1992–1997 (from Gosling, 1998).

(the observations were made by the Ulysses spacecraft between 1.4 and 5.4 AU heliocentric distances).

During solar minimum conditions the solar magnetic field is approximately dipole-like. The orientation of the dipole with respect to the solar rotation axis is quite variable. Near solar activity minimum the magnetic dipole tends to be nearly aligned with the rotation axis. The solar dipole is most noticeably tilted relative to the rotation axis during the declining phase of solar activity. The Sun's magnetic field is not dipole-like near solar activity maximum.

At times when the solar magnetic axis is substantially tilted with respect to the rotation axis the heliospheric current sheet becomes warped into a global structure that resembles a ballerina's twirling skirt. Earth crosses the current sheet at least twice during each solar rotation, sometimes more (if the current sheet is wavy enough). These current sheet crossings are observed at Earth as crossings of interplanetary magnetic sector boundaries, when the polarity of the interplanetary magnetic field changes its sign (as observed from Earth).

It is very important to note that active comets frequently have high inclination orbits. The plasma environment of these comets is quite different in the slow and in the fast solar wind. This point will be discussed in detail later in this paper.

5. Mass Loaded MHD Equations

There are several major ion species in the cometary plasma environment: ambient solar wind ions (mainly protons), heavy ions of cometary origin (mainly water group ions), and finally protons of cometary origin. In addition, the energetics of the electron population also exhibits a very complicated behavior.

Presently, global scale 3D models of the cometary plasma environment are single-fluid MHD models. This means that some of the underlying physics must be simplified, so that a single-fluid treatment can be used. The main simplifying assumptions are the following:

- Mass loading is dominated by the ionization of heavy cometary ions. A newly ionized heavy ion contributes about 20 times more mass to the mass density of charged particles than a newly ionized hydrogen atom. The mass loss due to charge exchange of ambient solar wind ions is also neglected.
- The pitch-angles of freshly ionized particles are assumed to be instantaneously scattered to an isotropic shell distribution (isotropic in the plasma frame). The flow velocities of implanted ions and the mass-loaded solar wind are assumed to be identical.
- Collisions (including charge exchange) between plasma particles and cometary neutrals do not change the plasma mass density. Even though this assumption is not strictly true, it represents a reasonable approximation which leads to great mathematical simplification.

In this section we show how these simplifying assumptions lead to the set of single-fluid equations which is solved in our model.

Based on our basic assumptions the conservation equations for the ambient solar wind have no significant sources and sinks:

$$\frac{\partial \rho_{sw}}{\partial t} + (\mathbf{u}\cdot\nabla)\rho_{sw} + \rho_{sw}(\nabla\cdot\mathbf{u}) = 0 \tag{1a}$$

$$\rho_{sw}\frac{\partial \mathbf{u}}{\partial t} + \rho_{sw}(\mathbf{u}\cdot\nabla)\mathbf{u} + \nabla p_{sw} = 0 \tag{1b}$$

$$\frac{\partial p_{sw}}{\partial t} + (\mathbf{u}\cdot\nabla)p_{sw} + \frac{5}{3}p_{sw}(\nabla\cdot\mathbf{u}) = 0 \tag{1c}$$

where t is time and ρ_{sw}, $\mathbf{u}$ and p_{sw} are the solar wind mass density, velocity and pressure.

The governing equation for the phase-space distribution function of implanted ions, F_c, can be written in the following form (cf. Gombosi, 1988):

$$\begin{aligned}\tfrac{\partial F_c}{\partial t} &+(\mathbf{u}\cdot\nabla)F_c + (\mathbf{v}\cdot\nabla)F_c \\ &-\left[\frac{\partial \mathbf{u}}{\partial t} + (\mathbf{u}\cdot\nabla)\mathbf{u} + (\mathbf{v}\cdot\nabla)\mathbf{u} - \frac{e}{m_c}(\mathbf{v}\times\mathbf{B})\right]\cdot\nabla_v F_c \\ &= \dot{n}_n\left[\delta^3(\mathbf{u}+\mathbf{v}-\mathbf{u}_n) - 2\,k_{in}\frac{\lambda}{u_n}(F_c - F_0)\right] - \alpha_e n_e F_c,\end{aligned} \tag{2}$$

here $\mathbf{u}_n$ is the cometary neutral gas bulk velocity, $\mathbf{v}$ is the implanted ion random velocity, $F_c(t, \mathbf{r}, \mathbf{v})$ is the implanted ion phase space distribution function in the plasma frame, e and m_c are the charge and mass of implanted ions, $\mathbf{B}$ is the magnetic field vector, and λ is the ionization scale length of cometary neutrals. Other quantities in (2) are the three dimensional Dirac delta function, δ^3, the ion-neutral momentum transfer collision rate, k_{in}, the production rate of cometary ions (due to photoionization of neutrals), $\dot{n}_n$, and the Maxwellian distribution function, F_0. Finally, the recombination coefficient, $\alpha_e n_e$, was discussed in detail in our previous paper (Gombosi et al., 1996).

The ion production rate due to photoionization is given by

$$\dot{n}_n = \frac{Q}{4\pi\lambda r_c^2} \exp\left(-\frac{r_c}{\lambda}\right). \tag{3a}$$

where Q is the cometary neutral gas production rate, r_c is cometocentric distance, and λ is the ionization scale-length of cometary neutrals.

The first two terms on the right hand side of Equation (2) describe the effects of ionization and ion-neutral collisions. The distribution function of scattered ions (see below), F_0, is given by Gombosi (1994):

$$F_0 = n_c \left(\frac{m_c}{2\pi k T_{cn}}\right)^{3/2} \exp\left[-\frac{m_c}{2kT_{cn}}(\mathbf{v} - \mathbf{u}_{cn})^2\right], \tag{3b}$$

where $n_c = \int \mathrm{d}^3 v F_c$ is the density of cometary pickup ions, while the temperature of the pickup population is defined as $T_c = (m_c/3kn_c) \int \mathrm{d}^3 v v^2 F_c$. The other quantities are given by

$$\mathbf{u}_{cn} = \frac{1}{2}(\mathbf{u} + \mathbf{u}_n) \tag{3c}$$

$$T_{cn} = \frac{1}{2}T_c + \frac{1}{12}\frac{m_c}{k}(\mathbf{u}_n - \mathbf{u})^2. \tag{3d}$$

In these formulas we assumed that the masses of cometary neutrals and pick-up ions are identical. The temperature of the cometary neutral exosphere is typically very low ($T_n < 100$ K), and in the present calculation the thermal motion of the neutral gas is neglected (cold gas approximation). In (2) the wave-particle interaction effects are also neglected.

The transport model to be used in this paper is a modified version of the model of Gombosi (1988, 1991), which assumes that the freshly ionized cometary particles form a pickup shell distribution in the magnetized solar wind plasma. Even though this assumption is not quite justified, it represents a reasonable first approximation and greatly simplifies the mathematical problem (see the discussion by Gombosi, 1991). This assumption means that the implanted ion distribution is

considered to be isotropic in the random velocity, $F_c = F_c(t, \mathbf{r}, v)$. In this case we obtain

$$\nabla_v F_c = \frac{\mathbf{v}}{v} \frac{\partial F_c}{\partial v}. \tag{4}$$

Substituting (4) into (2) leads to the following transport equation for the implanted ion distribution function:

$$\begin{aligned} &\frac{\partial F_c}{\partial t} + (\mathbf{u} \cdot \nabla) F_c + (\mathbf{v} \cdot \nabla) F_c \\ &\quad - \left[\frac{\partial \mathbf{u}}{\partial t} + (\mathbf{u} \cdot \nabla)\mathbf{u} + (\mathbf{v} \cdot \nabla)\mathbf{u} \right] \cdot \frac{\mathbf{v}}{v} \frac{\partial F_c}{\partial v} \\ &\quad = \dot{n}_n \left[\delta^3(\mathbf{u} + \mathbf{v} - \mathbf{u}_n) - 2 k_{in} \frac{\lambda}{u_n} (F_c - F_0) \right] - \alpha_e n_e F_c. \end{aligned} \tag{5}$$

It is important to note that (5) is independent of the magnetic field: this feature is a direct consequence of the directional isotropy of the velocity distribution.

Next, we multiply (5) by m_c, $m_c\mathbf{v}$, and $m_c v^2$, respectively, and integrate the resulting equations over the entire velocity space. This operation results in the following set of moment equations for the implanted cometary ions:

$$\frac{\partial \rho_c}{\partial t} + (\mathbf{u} \cdot \nabla)\rho_c + \rho_c(\nabla \cdot \mathbf{u}) = \dot{\rho} - \alpha_e n_e \rho_c \tag{6a}$$

$$\rho_c \frac{\partial \mathbf{u}}{\partial t} + \rho_c(\mathbf{u} \cdot \nabla)\mathbf{u} + \nabla p_c = \dot{\rho}\,(1 + \eta_c\,\rho_c)\,(\mathbf{u}_n - \mathbf{u}), \tag{6b}$$

$$\begin{aligned} &\frac{\partial p_c}{\partial t} + (\mathbf{u} \cdot \nabla) p_c + \frac{5}{3} p_c(\nabla \cdot \mathbf{u}) \\ &\quad = \frac{1}{3}\,\dot{\rho}\,\left[(1 + \eta_c\,\rho_c)(\mathbf{u}_n - \mathbf{u})^2 - 3\eta_c\,p_c\right] - \alpha_e n_e p_c, \end{aligned} \tag{6c}$$

where the mass addition rate $\dot{\rho}$ and the ion-neutral friction coefficient η_c are given by

$$\dot{\rho} = \frac{m_c\,Q}{4\pi\,\lambda r_c^2} \exp\left(-\frac{r_c}{\lambda}\right) \tag{7a}$$

$$\eta_c = \frac{\lambda}{m_c} \frac{k_{in}}{u_n}. \tag{7b}$$

Next we introduce the total mass density and pressure by $\rho = \rho_{sw} + \rho_c$ and $p = p_{sw} + p_c$. The governing equations for these quantities can be obtained by adding the conservation equations for the solar wind and implanted ions:

$$\frac{\partial \rho}{\partial t} + \nabla \cdot (\rho\,\mathbf{u}) = \dot{\rho} - \alpha_e n_e \rho \tag{8a}$$

$$\frac{\partial(\rho\,\mathbf{u})}{\partial t} + \nabla\cdot\left(\rho\,\mathbf{u}\,\mathbf{u} + p\,I + \frac{B^2}{2\mu_0}\,I - \frac{\mathbf{B}\,\mathbf{B}}{\mu_0}\right) = \dot{\rho}\,\left[\mathbf{u}_n + \eta_c\,\rho\,(\mathbf{u}_n - \mathbf{u})\,\right] - \alpha_e n_e \rho \mathbf{u}, \tag{8b}$$

$$\frac{\partial}{\partial t}\left(\frac{1}{2}\,\rho\,u^2 + \frac{3}{2}p + \frac{B^2}{2\mu_0}\right) + \nabla\cdot\left(\frac{1}{2}\,\rho\,u^2\mathbf{u} + \frac{5}{2}p\,\mathbf{u} + \frac{(\mathbf{B}\cdot\mathbf{B})\,\mathbf{u} - \mathbf{B}\,(\mathbf{B}\cdot\mathbf{u})}{\mu_0}\right) = \frac{1}{2}\,\dot{\rho}\,\left[u_n^2 + \eta_c\,\rho\,(u_n^2 - u^2) - 3\eta_c\,p\right] - \alpha_e n_e \frac{1}{2}\left(\rho\,u^2 + 3p\right), \tag{8c}$$

$$\frac{\partial\,\mathbf{B}}{\partial t} + \nabla\cdot(\mathbf{u}\,\mathbf{B} - \mathbf{B}\,\mathbf{u}) = 0, \tag{8d}$$

where ρ, $\mathbf{u}$, and p are the mass density, velocity and pressure of the mass loaded plasma. In Equation (8b) I represents the 3×3 unit matrix, while μ_0 is the permeability of vacuum.

It should be noted that in the present model the flow velocities of the solar wind plasma and of the implanted cometary ions are assumed to be the same. This assumption makes it possible to combine the two sets of transport equations and obtain a full set of flow equations for the mass loaded plasma flow.

6. Numerical Solution

Recently we developed a new numerical method which solves the equations of ideal magnetohydrodynamics on a solution-adaptive Cartesian mesh using a second-order MUSCL-type numerical method. We call our new method *Multiscale Adaptive Upwind Scheme for Magnetohydrodynamics* (MAUS-MHD).

MAUS-MHD is built from two pieces that are extremely well suited to the cometary mass-loading problem. The first is a data structure that allows for adaptive refinement of the mesh in regions of interest (DeZeeuw and Powell, 1992), and the second is a second-order MUSCL-type scheme (van Leer, 1979) based on a new approximate Riemann solver for ideal MHD. The details of the new numerical method have already been published in several papers (Gombosi et al., 1994, 1996; Powell, 1994; Powell et al., 1995) and a comprehensive description of the entire method is presently in preparation (Powell et al., 1999).

6.1. DATA STRUCTURE

Adaptive refinement and coarsening of a mesh is a very attractive way to make optimal use of computational resources. It becomes particularly attractive for problems in which there are disparate spatial scales. For problems like the cometary mass-loading problem, in which the ionization length scale and the radius of the comet differ by several orders of magnitude, an adaptive mesh is a virtual necessity. The primary difficulty in implementing an adaptive scheme is related to the way in which the solution data are stored; the data structure must be much more flexible than the simple array-type storage used in the majority of scientific computations.

The basic data structure used is a hierarchical cell-based octree structure — "parent" cells are refined by division into eight "children" cells. Each cell has a pointer to its parent cell (if one exists) and to its eight children cells (if they exist). The "leaves of the tree", that is, the cells with no children, are the cells on which the calculation takes place.

This tree structure contains all the connectivity information necessary to carry out the flow calculations; no other connectivity information is stored. While it involves a more sophisticated implementation than a simple array-type data structure, it is an efficient and natural way to implement adaptive refinement and coarsening.

The mesh is generated in such a way that important geometric and flow features are resolved. The geometry is resolved by recursively dividing cells in the vicinity of the comet until a specified cell-size is obtained. A larger cell-size is specified for the remainder of the mesh. Flow features are resolved by obtaining a solution on this original mesh, and then automatically refining cells in which the flow gradients are appreciable, and coarsening cells in which the flow gradients are negligible. This is done by evaluating $|\nabla \cdot \mathbf{u}|$, $|\nabla \times \mathbf{u}|$ and $|\nabla B|$ in each cell, and refining cells in which any of the three is large, and coarsening cells in which all of the three are small.

The resulting grid has small cells next to larger cells. A numerical procedure that is both accurate and stable on a mesh of this type cannot be developed from simple finite difference ideas but must be based on techniques developed for unstructured meshes. The gradient calculation procedure that makes the scheme second order, and the limiting procedure that renders it monotonicity preserving, are described elsewhere (DeZeeuw and Powell, 1992).

Basically, the scheme is a finite volume scheme, in which the governing equations are integrated over a cell of the mesh. This way the governing equations given by equations (8a) through (8d) become a set of coupled ordinary differential equations in time, which can be solved by a suitable numerical integration procedure. In MAUS-MHD, an optimally smoothing multistage scheme (van Leer et al., 1989) is used. To carry out the multistage time-stepping procedure for equations (8a) through (8d), an evaluation of the flux tensor at the interfaces between cells of the mesh (a so called "Riemann solver") is required.

6.2. RIEMANN SOLVER

Previous upwind-based schemes for MHD (Brio and Wu, 1988; Zachary and Collella, 1992) have been based on the one-dimensional Riemann problem obtained by noting that, for one-dimensional problems, the $\nabla \cdot \mathbf{B} = 0$ condition reduces to the constraint that $B_x = \text{const}$. This allows the fifth row and column of the Jacobian matrix to be dropped, yielding a 7×7 system. Applying schemes based on this one-dimensional Riemann problem to MHD problems in more than one dimension leads to a serious problem, however. Because there is no evolution equation for the component of the magnetic field normal to a cell face, a separate procedure for updating this portion of the magnetic field must be implemented, and must be implemented in such a way as to meet the $\nabla \cdot \mathbf{B} = 0$ constraint. Typically, this is done by the use of a projection scheme (Zachary and Collella, 1992; Tanaka,1993).

In MAUS-MHD a new approach is taken (Powell, 1994; Powell et al., 1995). It is based on the observation that one can derive the equations of ideal MHD without explicitly using the $\nabla \cdot \mathbf{B} = 0$ equation. This yields the set of equations

$$\frac{\partial \mathbf{W}}{\partial t} + (\nabla \cdot \mathbf{F})^T = \mathbf{S} + \mathbf{P} - \mathbf{L}, \tag{9}$$

where the T exponent symbolizes a transposed matrix. The state vector, $\mathbf{W}$, and the flux diad, $\mathbf{F}$, are defined as

$$\mathbf{W} = \begin{pmatrix} \rho \\ \rho\,\mathbf{u} \\ \mathbf{B} \\ \frac{1}{2}\rho\mathbf{u}\cdot\mathbf{u} + \frac{3}{2}p + \frac{1}{2\mu_0}\mathbf{B}\cdot\mathbf{B} \end{pmatrix}, \tag{10a}$$

$$\mathbf{F} = \begin{pmatrix} \rho\,\mathbf{u} \\ \rho\,\mathbf{u}\,\mathbf{u} + \left(p + \frac{1}{2\mu_0}\mathbf{B}\cdot\mathbf{B}\right)\mathbf{I} - \frac{1}{\mu_0}\mathbf{B}\mathbf{B} \\ \mathbf{u}\mathbf{B} - \mathbf{B}\mathbf{u} \\ \mathbf{u}\left(\frac{1}{2}\rho\mathbf{u}\cdot\mathbf{u} + \frac{5}{2}p + \frac{1}{\mu_0}\mathbf{B}\cdot\mathbf{B}\right) - (\mathbf{B}\cdot\mathbf{u})\,\mathbf{B} \end{pmatrix}^T, \tag{10b}$$

where μ_0 is the permeability of vacuum. Finally, $\mathbf{S}$, $\mathbf{P}$ and $\mathbf{L}$ are given by

$$\mathbf{S} = -\nabla \cdot \mathbf{B} \begin{pmatrix} 0 \\ \frac{1}{\mu_0}\mathbf{B} \\ \mathbf{u} \\ \frac{1}{\mu_0}\mathbf{B}\cdot\mathbf{u} \end{pmatrix}, \tag{10c}$$

$$\mathbf{P} = \dot{\rho} \begin{pmatrix} 1 \\ \left[\mathbf{u}_n + \eta_c\,\rho\,(\mathbf{u}_n - \mathbf{u})\right] \\ 0 \\ \frac{1}{2}\left[u_n^2 + \eta_c\,\rho\,(u_n^2 - u^2) - 3\eta_c\,p\right] \end{pmatrix}, \tag{10d}$$

$$\mathbf{L} = \alpha_e n_e \begin{pmatrix} \rho \\ \rho\,\mathbf{u} \\ \mathbf{0} \\ \frac{1}{2}\rho\,u^2 + \frac{3}{2}p \end{pmatrix}. \tag{10e}$$

A Riemann solver based on these eight equations, as shown in (Gombosi et al., 1994, 1996); Powell, 1994; Powell et al., 1995), has substantially better numerical properties than one based on the form in which the source term **S** is dropped. The Riemann solver based on Equation (9) gives a consistent update for the component of the magnetic field normal to a cell face, such that the resulting numerical scheme treats $(\nabla \cdot \mathbf{B})/\rho$ as a passive scalar. Now any $(\nabla \cdot \mathbf{B})/\rho$ that is created numerically is passively convected, and, in the steady state, $(\nabla \cdot \mathbf{B})/\rho$ is constant along streamlines. In this treatment $\nabla \cdot \mathbf{B} = 0$ is satisfied to within truncation error, once it is imposed as an initial condition to the problem. The resulting scheme is stable to these truncation-level errors in the divergence of **B**, and does not require a projection scheme.

Given the eigenvalues and right eigenvectors of Equation (9) (Gombosi et al., 1994, 1996; Powell, 1994; Powell et al., 1995), the flux through an interface is given by

$$\Phi\,(\mathbf{W}_L, \mathbf{W}_R) = \frac{1}{2}\,(\Phi_L + \Phi_R) - \frac{1}{2}\sum_{k=1}^{8} |\lambda_k|\,\alpha_k \mathbf{R}_k \tag{11}$$

where λ_k and $\mathbf{R}_k$ are the kth eigenvalue and right eigenvector (these can be found in Gombosi et al., 1994; Powell, 1994; Powell et al., 1995), α_k is the inner product of the kth left eigenvector with the state difference, $\mathbf{W}_R - \mathbf{W}_L$, while the quantities, Φ_L and Φ_R, are simply $\mathbf{F}(\mathbf{W}_L) \cdot \mathbf{n}$ and $\mathbf{F}(\mathbf{W}_R) \cdot \mathbf{n}$, respectively.

The advantages of the flux-based approach described above are:

1. The flux function is based on the eigenvalues and eigenvectors of the Jacobians of **F** with respect to **W**, leading to an upwind-differencing scheme which respects the physics of the problem being solved,

2. The scheme provides capturing of shocks and other high-gradient regions without oscillations in the flow variables,

3. The scheme has just enough dissipation to provide a nonoscillatory solution, and no more,

4. The scheme provides a physically consistent way to implement boundary conditions that are stable and accurate: a physically consistent flux can be calculated at the far-field boundaries by use of the approximate Riemann solver.

7. Comet Hale–Bopp

Comet Hale–Bopp (C/1995 O1) is the largest and most active comet seen in modern times. Because of this and the capabilities of the latest state-of-the-art observatory

instrumentation, high quality science measurements have been and are being made covering an unprecedented range of heliocentric distances out to nearly 7 AU. The first gaseous emission detected was that of CN when the comet was 6.82 AU from the Sun (Fitzsimmons and Cartwright, 1996). The emission of CO was detected spectroscopically in the sub-mm when the comet was 6.5 AU from the Sun (Jewett et al., 1996). CO was then probably the dominant gas species in the coma. Water production was detected through OH observations in the radio (Biver et al., 1997) and in the UV from HST and IUE (Weaver et al., 1997), and from the ground (Schleicher et al., 1997) once the comet was closer than about 5 AU from the Sun. Water did not become the dominant species, however, until the comet reached about 3.5 AU. As Hale–Bopp moved closer to the Sun in mid-August 1996 ion emission features of CO^+ (Jockers et al., 1996) and H_2O^+ (Rauer et al., 1997) were observed when the comet was at 3.3 AU from the Sun. For typical bright comets, the ion tail emissions are not normally detectable until comets are within about 1.5 to 2 AU.

Extrapolations of preperihelion observations (Weaver et al., 1997; Biver et al., 1997) indicated a likely water production rate approaching 10^{31} molecules/s near perihelion. Preliminary analysis of hydrogen coma measurements (Bertaux, private communication) taken by the Solar Wind Anisotropies (SWAN) experiment on the Solar and Heliospheric Observatory (SOHO) is consistent with this projection.

8. 3D MHD Simulation of the Solar Wind Interaction with Comet Hale–Bopp

Equation (9) was solved in dimensionless quantities for comet Hale–Bopp. The parameters reflect conditions for April 11, 1997, when the comet was actively observed post perihelion. Because at this time the comet was near the solar wind streamer belt, two sets of simulations were carried out describing the interaction of the comet with slow and fast solar wind streams. In order to keep the differences between the two runs to a minimum we kept the solar wind density constant for both the slow and fast streams (even though observations indicate that the solar wind flux is quite similar in fast and slow streams).

The parameter values used in the present calculations are summarized in Table I. In addition, we used the same recombination rate as in our previous simulations (Gombosi et al., 1996). The electron temperature was assumed to be half of the plasma temperature. This assumption makes it possible to calculate the recombination rate self-consistently in a single-fluid simulation.

At the boundaries of the simulation box (25 million km in the upstream, 50 million km in the downstream and perpendicular directions) free streaming solar wind conditions were applied, while the source and loss terms were applied inside the simulation domain. The use of such a large simulation box is very important to ensure that our results are not controlled by the way boundary conditions were implemented.

TABLE I
Physical parameters used in the present simulations

Quantity	Symbol	Value	Units
Heliocentric distance	d	0.93	AU
Heliolatitude	δ	32	Degrees
IMF magnitude	B_∞	4.81	nT
IMF angle		24	Degrees
Specific heat ratio	γ	5/3	
Solar wind number density	n_{sw}	5	cm^{-3}
Mean molecular mass of solar wind ions	m_{sw}	1	amu
Solar wind plasma temperature	$T_{sw} = T_i + T_e$	10^5	K
Sound speed in solar wind	a_∞	37.1	km s^{-1}
Slow solar wind speed	u^s_{sw}	371	km s^{-1}
Slow solar wind acoustic Mach number	M^s_∞	10	
Slow solar wind Alfvénic Mach number	$M^s_{A\infty}$	7.9	
Fast solar wind speed	u^f_{sw}	742	km s^{-1}
Fast solar wind acoustic Mach number	M^f_∞	20	
Fast solar wind Alfvénic Mach number	$M^f_{A\infty}$	15.8	
Gas production rate	Q	10^{31}	Molecules s^{-1}
Ionization scale length	λ	10^6	km
Mean molecular mass of cometary ions	m_c	17	amu
Ion-neutral momentum transfer collision rate	k_{in}	1.7×10^{-9}	cm^3 s^{-1}

As a result of the careful use of grid coarsening and refining, the total number of grid points in this 3D MHD calculation is only about 300 000 with 13 levels of adaptive refinement. The solution contains far, far more detail than a solution from a nonadapted grid of $70 \times 70 \times 70$, which would require approximately the same amount of memory and CPU time to compute.

Figure 2 shows the final grid structure under steady-state conditions. The left panel shows the full simulation box (75 Mkm $\times$ 50 Mkm $\times$ 50 Mkm), the upper right panel shows the grid structure in the shock region, while the lower right panel shows the mesh in the inner coma near the diamagnetic cavity. Distances are meas-

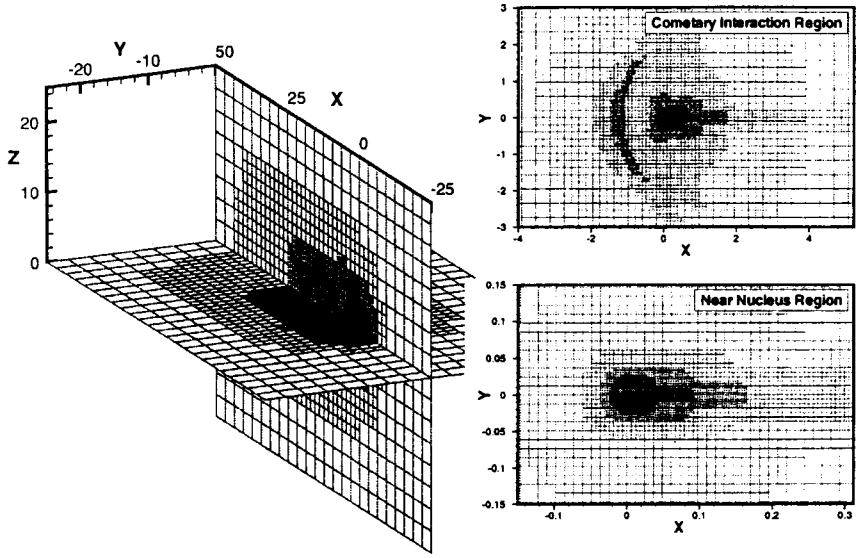

Figure 2. The self-adapted computational mesh used in the simulation. All distances are given in units of 10^6 km.

ured in units of 10^6 km. The largest and smallest cell sizes are $(3.125 \times 10^6\,\mathrm{km})^3$ and $(763\,\mathrm{km})^3$ with 13 levels of refinement in the calculation. The grid shows the shock region and the inner coma, where the diamagnetic cavity is formed.

The $-x$ axis points towards the Sun along the Sun-comet line. The y axis was chosen in a way that the (x,y) plane contains the interplanetary magnetic field line (in this case it is the nominal Parker spiral). Finally, the z axis completes a right-handed coordinate system.

Figure 3 shows a 3D composite representation of several physical quantities for fast solar wind conditions. The Figure shows an approximately 20 Mkm segment of the cometary interaction region. The grid structure is shown in the equatorial plane (horizontal plane) and the noon-midnight meridian (vertical plane). "Equatorial plane" here refers to the plane containing the interplanetary magnetic field lines. The grayscale code represents the kinetic pressure of the plasma flow: dark corresponds to the pressure in the free streaming solar wind, while white represents an approximately 200 times higher pressure. Black lines in the equatorial plane represent magnetic field lines, while white lines in the noon-midnight meridian show plasma flow lines.

Inspection of Figure 3 reveals the well established large-scale properties of the cometary interaction region. The supersonic solar wind slows down from its upstream Mach number of $M = 20$ to about $M = 2$ before the shock is formed due to mass loading. The subsolar distance of the shock is $\sim 1.6 \times 10^6$ km for slow and $\sim 1.2 \times 10^6$ km for fast solar wind conditions. Each newly implanted heavy cometary ion contributes $m_c u^2/3$ to the plasma pressure, which means that

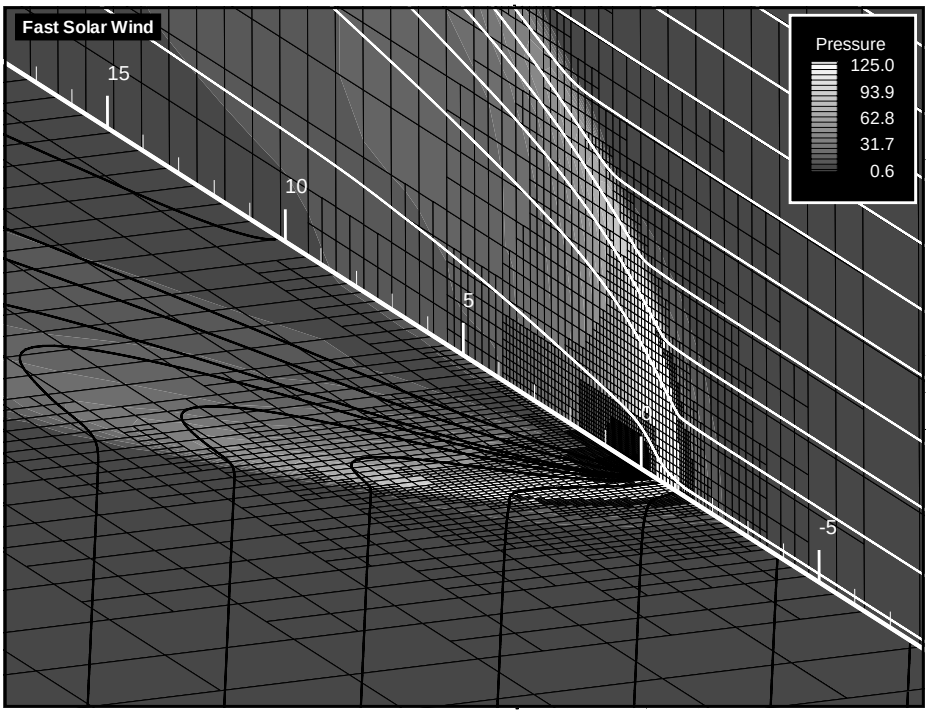

Figure 3. 3D plot of the cometary interaction region. All distances are given in units of 10^6 km.

upstream of the shock most of the mass density is still in the solar wind protons, but the pressure is gradually dominated by cometary pickup ions. In this upstream region the flow is somewhat slowed down by mass loading, but the main effect is a considerable increase of the pressure, which greatly reduces the Mach number. The result of the large mass loading is that the supersonic plasma flow "senses" the presence of the comet well ahead of the shock. However, the reason is not that information propagates upstream in a supersonic flow, but rather the background medium changes far upstream of the comet. In any case, this situation is quite unusual in fluid dynamics and it represents a fundamentally new kind of interaction between the solar wind and a solar system body.

The large-scale behavior of the magnetic field lines and plasma flow lines is also well understood in terms of earlier theoretical work and *in situ* observations (cf. Gombosi et al., 1996). In the equatorial plane the interplanetary magnetic field (IMF) lines are draped around the comet. This draping takes place because the plasma flow becomes very slow in the densest regions of the inner coma and therefore the convected magnetic field will "hang-up" in this region. In the undisturbed solar wind the IMF vector has no out of plane component, therefore the largest field line "draping" occurs in the equatorial plane. The field lines must "slip" around the innermost coma in order to get past the near-nucleus region. It can be seen in Figure 3 that the field lines are still highly draped behind the nucleus and they form

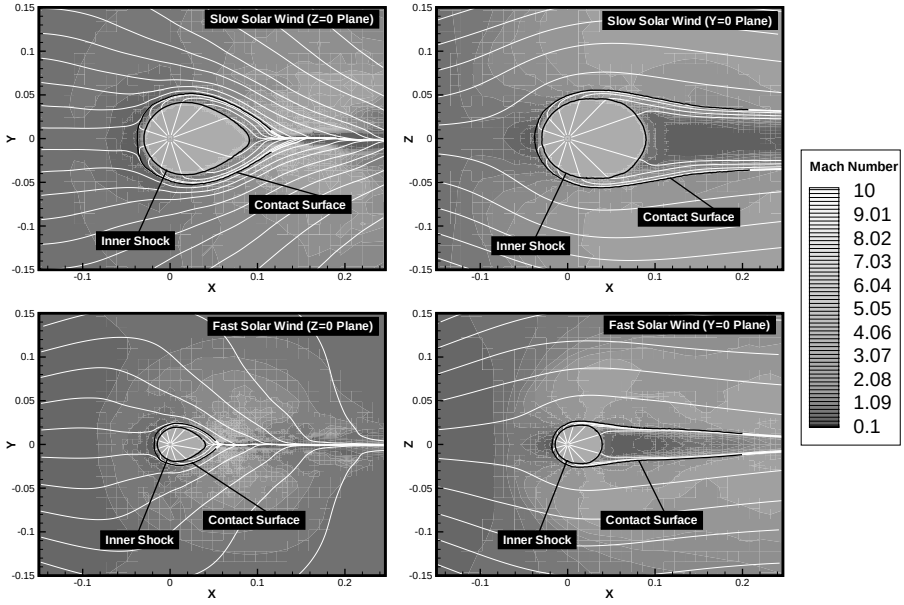

Figure 4. Color coded Mach number values and plasma stream lines (white lines) in the inner coma. All distances are given in units of 10^6 km.

the cometary plasma tail. Several million km downstream the field lines gradually recover their original shape due to the "pull" of the undisturbed solar wind in the distant flanks.

In the outer coma the mass loading is the dominant physical process which controls the large-scale behavior of the cometary plasma environment. In the inner coma, however, several physical processes play important roles and the resulting plasma structure is controlled by an interplay between these processes.

Our model includes the major physical processes believed to play important roles in the inner coma plasma environment: continuous mass loading, recombination, and last but not least, ion-neutral friction.

Figure 4 shows the plasma flow in the inner coma. The enlarged region is about 300 000 km $\times$ 150 000 km, which is about 50 times smaller than the region shown in Figure 3, demonstrating the ability of our adaptive grid to resolve vastly different scales. The grayscale code represents the Mach number, the white lines are plasma stream lines, and finally, thick black lines denote plasma boundaries (to be discussed below).

Inspection of Figure 4 reveals several very interesting features in the inner coma. It can be seen that there are two clearly separated plasma flows in the near nucleus region. At larger distances from the nucleus the plasma is basically a heavily mass

loaded, slow solar wind flow. On the dayside the flow lines are diverted around the dense inner region and later converge into the wake region.

The cold plasma in the dense near nucleus region consists exclusively of ionized cometary molecules and it is strongly coupled to the radially expanding neutral atmosphere via ion-neutral collisions. Due to this strong coupling the velocity of this outward flowing plasma is about the same as the neutral gas velocity ($\sim$1 km s^{-1}). Also, as a result of the very low plasma temperature, this expanding flow is supersonic.

The interaction between the radially expanding "ionospheric" plasma and the contaminated, nearly stagnating solar wind flow has been extensively discussed in the past. The formation of a contact surface and an "inner shock" was predicted theoretically in order to divert the ionospheric plasma flow toward the tail and avoid interpenetration between the ionospheric and solar wind plasmas (Mendis et al., 1985). Also, as a result of recombination of the shocked ionospheric plasma in the subsolar region, the inner shock can move very close to the boundary separating the two plasma flows (Cravens, 1989). This phenomenon was observed at comet Halley (Goldstein et al., 1989). It was also predicted, that due to the separation of the "ionospheric" and solar wind plasmas no magnetic field can penetrate inside the contact surface, thus creating a "diamagnetic cavity".

Our simulation results are not only completely consistent with the theoretical predictions, but they also reveal many new details of the plasma cavity and near tail regions. It can be seen in Figure 4 that the teardrop shaped inner shock is elongated towards the the tail. On the dayside its subsolar distance is about 3×10^4 km for slow solar wind and $\sim 1.5 \times 10^4$ km for fast solar wind conditions (we note that for comet Halley the comparable distance was about 2200 km). It is interesting to note that the inner shock is terminated by a Mach disk near the antisolar point. This structure is entirely consistent with the "point source" nature of the ionospheric plasma flow (Wallis and Dryer, 1976).

Behind the terminator the external plasma flow lines "converge" toward the sun-comet axis. This "pinching" effect is well known in planetary magnetospheres and it is a consequence of the pressure gradient perpendicular to the axis of the cometary wake. In effect, the plasma is filling the "void" created by the cometary obstacle (which basically corresponds to the diamagnetic cavity). The outermost black line in Figure 4 denotes the last solar wind flow line (this separatrix is the contact surface between flow lines in the solar wind and in the ionosphere). This separatrix is the outer edge of the cometary plasma cavity boundary layer. It is interesting to note that the region inside the separatrix narrows considerable on the nightside due to the inflow of the outside plasma into the cometary wake. This converging boundary forces the shocked cometary ionospheric flow into the plasma tail through a narrow nozzle, and consequently, accelerates the plasma towards the tail.

It is interesting to note that the diamagnetic cavity is basically constrained to the region within the inner shock. Since the ionospheric outflow inside the inner shock

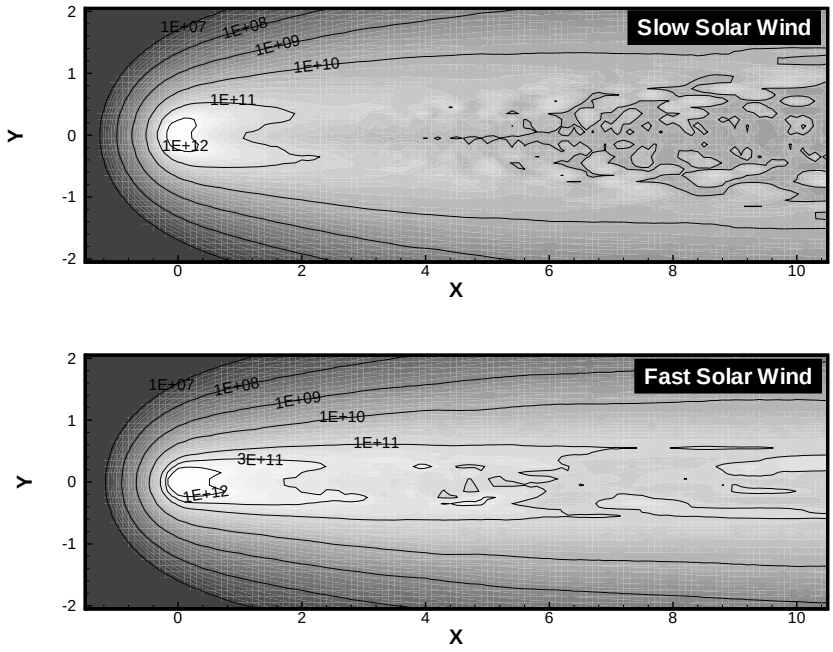

Figure 5. Synthetic H_2O^+ images. All distances are given in units of 10^6 km.

is supersonic, the magnetic field cannot diffuse upstream through the inner shock. On the dayside the inner shock is quite close to the inner edge of the cometary plasma cavity boundary layer, and the magnetic field is practically negligible inside this region. Behind the terminator, however, a weak magnetic field penetrates into the region between the inner shock and the cometary plasma cavity boundary layer and this region becomes the inner end of the cometary plasma tail.

9. Simulation of H_2O^+ and CO^+ Emissions

The observation of ions created by ionization of cometary gas, either by ground-based observations or by in situ measurements can give us useful information about the gas production and composition of comets. However, due to the interaction of ions with the magnetized solar wind and their high chemical reactivity, it is not possible to relate measured ion densities (or column densities) directly to the parent gas densities. In order to quantitatively analyze measured ion abundances in cometary comae it is necessary to understand their dynamics and chemistry.

We have recently developed a detailed ion-chemical network of cometary atmospheres (Häberli et al., 1997b). We include production of ions by photo- and electron impact ionization of a background neutral atmosphere, charge exchange

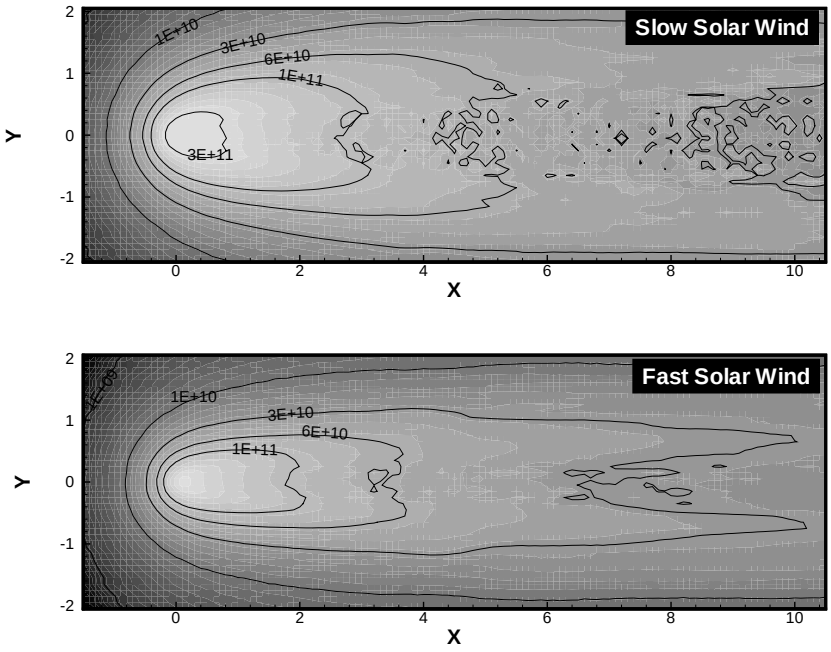

Figure 6. Synthetic CO^+ images. All distances are given in units of 10^6 km.

of solar wind ions with cometary atoms/molecules, reactions between ions and molecules, and dissociative recombination of molecular ions with thermal electrons. By combining the ion-chemical network with the three-dimensional plasma flow as computed by our fully three-dimensional MHD model of cometary plasma environments (described above) we are able to compute the density of the major cometary ions everywhere in the coma. The input parameters for our model are the solar wind conditions (density, speed, temperature, magnetic field) and the composition and production rate of the gas.

We have applied our model to comet Hale–Bopp on April 11, 1997, for which the input parameters are reasonably well known. In Figures 5 and 6 we present synthetic images (as seen from Earth) of the resulting column densities of H_2O^+ and CO^+ for slow and fast solar wind conditions. The results of our model can be directly compared with both the spatial distribution and the absolute abundance of H_2O^+ and CO^+ and with with the overall water production rate.

We have compared the H_2O^+ model results shown in Figure 5 with two preliminary reductions of comet Hale–Bopp data sets. The synthetic H_2O^+ image for the fast-stream model compares very well with an observed H_2O^+ taken by Wilson and Mendillo (personal communication) for similar conditions to our model at nearly the corresponding time before perihelion. The model accurately reproduces the observed brightness, its variation with distance down the tail, and the bifurcated

structure of the tail. The bifurcation of the H_2O^+ tail was explained in terms of the analysis of the VEGA-flyby period Halley observations by Häberli et al. (1997b). The agreement in absolute brightness also appears to be consistent with the corrected value for the (8-0) band g-factor explained by Häberli et al. (1997b). A detailed comparison of our simulations and observations will be the subject of a separate study.

We also compared our model results with line-of-sight average velocities determined by Anderson (1997) from observations of many individual lines of the (8-0) band of H_2O^+ using the Hydra spectrograph on the WIYN (Wisconsin, Indiana, Yale, NOAO) Telescope. Hydra enables moderately high-resolution spectra to be measured at an adjustable array of points in the image plane of the telescope, corresponding to multiple locations in the coma and tail of the comet. Observations were made at sets of point on a few concentric rings around the head of the comet, and at selected points up to $\sim$20 arc minutes down the tail of the comet. The observations were taken when comet Hale–Bopp was traversing intermediate heliocentric latitudes where the Ulysses spacecraft found the solar wind conditions oscillates rapidly between fast (800 km s^{-1}) and slow 400 km s^{-1} streams. A comparison between the model results and the observations indicates the upstream region, the head of the comet, is indicative of slow solar wind conditions, but the fast velocities down the tail are indicative of the fast solar wind. Slow measured velocities upstream are consistent with the larger values for the bow shock and contact surface expected for a slow solar wind type of interaction. Fast speeds out in the tail are more consistent with the smaller values for the bow shock and contact surface expected for the fast solar wind type of interaction. It is quite possible that the observations were made at time when the head of the comet was instantaneously in the recent switch to the slow solar wind regime but the plasma in the tail was formed and accelerated earlier in a fast solar wind stream.

10. Simulation of Cometary X-ray Emission

Observations of comet C/Hyakutake by the Röntgen x–ray satellite ROSAT have revealed the emission of soft x–rays from the coma at an unexpected high level of about 10^{25} photons s^{-1} (Lisse et al., 1996). There is still no clear winner among the proposed production mechanisms (charge exchange between cometary neutrals and high charge state solar wind minor ions, scattering of solar x–rays by attogram dust particles, electron bremsstrahlung radiation, spectral line radiation from electron impact and recombination excitation). However, recent observational evidence seems to favor Cravens' (1997) charge exchange excitation (CXE) mechanism (Dennerl et al., 1997; Mumma et al., 1997). Here we present synthetic x–ray images calculated with the CXE mechanism. The method was described in our Hyakutake x–ray paper (Häberli et al., 1997a).

Cravens (1997) proposed that the observed x–ray emission is caused by charge exchange excitations of high charge state solar wind ions (O^{7+}, O^{6+}, C^{6+}, etc.) with neutral molecules/atoms such as $O^{7+} + H \rightarrow O^{6+*} + H^{+}$. The electron is most likely captured into an excited state of the solar wind minor ion, leading to emission of soft x–ray and EUV radiation. This process is known to be very efficient and is often used as a diagnostic tool to monitor low–Z elements in laboratory plasmas.

Using our 3D AMR MHD model we have calculated the solar wind velocity and streamlines in the coma for comet Hale–Bopp (for April 11, 1997). These simulations were described earlier in this paper. The densities of the major heavy ($Z > 2$) solar wind ions are computed by integrating the coupled system of continuity equations along the streamlines using the vector flow field from the MHD calculation. The production or loss of a particular species by charge exchange with cometary gas is taken into account as source terms to the equations. We include charge exchange with the cometary species H, O, H_2O, OH, and CO to calculate the cascading from high to low charge states.

In the case of CXE of a fully stripped ion X^{q+} with an atom/molecule of similar ionization potential as H, the excited state population of the $X^{(q-1)+}$ ion will be peaked around $n = q^{0.75}$. The distribution of excited states is very narrow at low encounter speeds, but broadens at energies above 10 keV/amu (15). Since the energy of relative motion in our case will be at or below 1 keV/amu we assume that all electrons get captured into a shell with $n \simeq q^{0.75}$. We assume the same behavior for non–fully stripped ions, in this case, n is increased by 1 if the lowest shell is already occupied by electrons. For intermediate n levels the excitation takes place into the highest angular momentum state. It is therefore expected, based on atomic selection rules, that the de–excitation takes place primarily in transitions of $\Delta n = 1$. Detailed calculations indeed show, that $\Delta n = 1$ transitions are more probable than $\Delta n = 2$ transitions by a factor of 5 to 10 at X-ray and EUV wavelengths. It is therefore well justified to assume that the de-excitation of the excited ions occurs *only* in steps of $\Delta n = 1$. This simplification assures that the calculated overall x–ray intensity is quite realistic, but the energy spectrum is somewhat oversimplified. More detailed calculations would result in a large number of spectral lines in the EUV and soft x–ray spectral regions.

Using the calculated densities of the solar wind ions in the coma we have computed the rate of CXE for every species and the corresponding volume emission rate of photons. By integrating the volume emission rate along the line–of–sight we obtained the synthetic images shown in Figure 7. The computed image has a crescent like shape with the maximum displaced from the nucleus by about 200 000 km along the Sun–comet line. The crescent shape is caused by the depletion of solar wind ions due to charge exchange when approaching the comet.

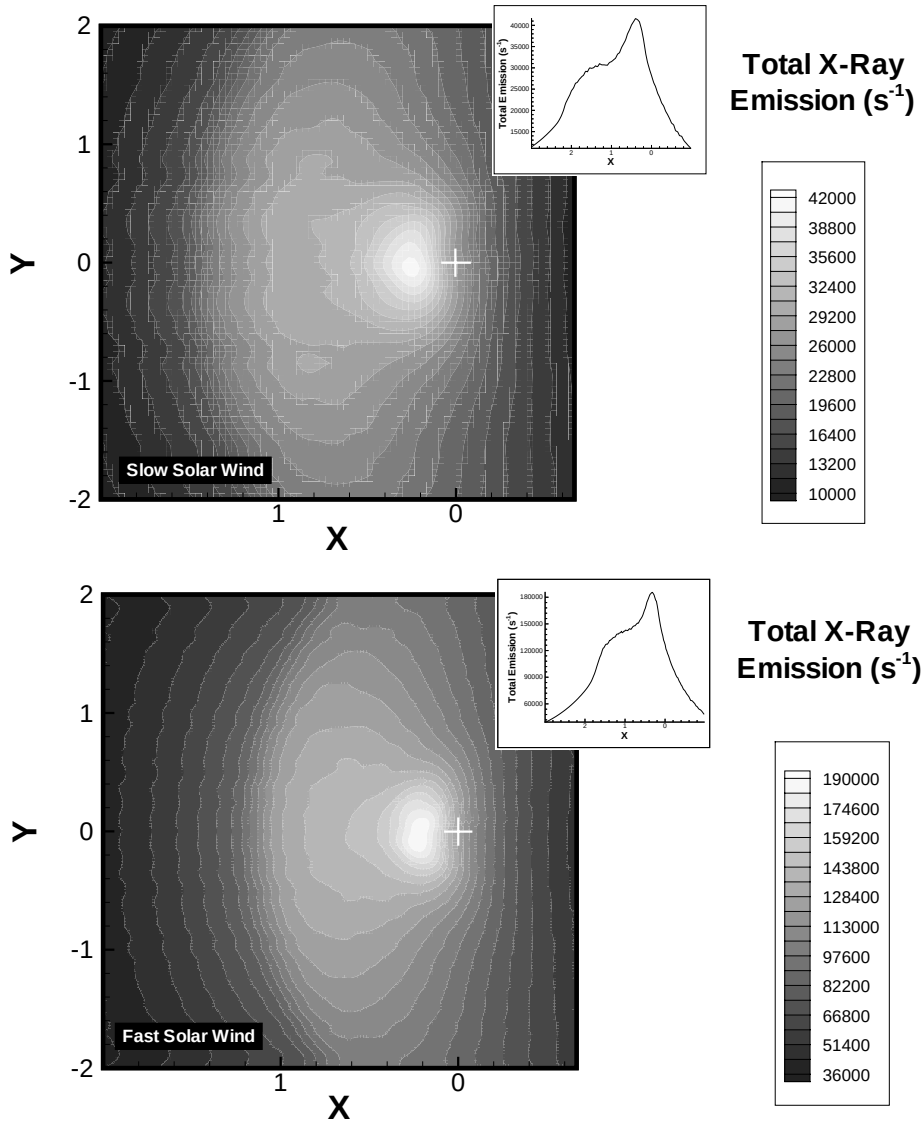

Figure 7. Synthetic soft x-ray images. All distances are given in units of 10^6 km.

11. Summary

Simulation results obtained with our new 3D multiscale MHD model are presented for comet Hale–Bopp. The unprecedented high production rate represents a particular computational challenge for simulations, since the spatial scales in the cometary magnetospheres are unusually large.

Our adaptive mesh simulations resolve all important plasma regions in the magnetosphere of Comet Hale–Bopp. We not only capture the cometary shock as well as the diamagnetic cavity boundary region and the inner shock, but also resolve the long plasma tail.

The simulation was also used to produce synthetic H_2O^+, CO^+ and soft x–ray images as seen from Earth on April 11, 1997. Since at this time the comet was near the high-latitude edge of the solar wind streamer belt, simulations for both slow and fast solar wind conditions were performed. In the future our synthetic images can directly be compared with observations.

This work was supported by NASA under grants NAG5–4714, NAGW–1366, and NCCS5–146 and by NSF under grants AST–9618795 and ATM–9318181.

References

A'Hearn, M. F. and Festou, M. C.: 1990, 'The Neutral Coma', in W. F. Huebner (ed.), *Physics and Chemistry of Comets*, Springer-Verlag, Berlin, p. 69.

A'Hearn, M. F., Hoban, S., Birch, P. V., Bowers, C., Martin, R., and Klingleshmith, D. A.: 1986, 'Cyanogen Jets in Comet Halley', *Nature* **324**, 649.

Altwegg, K., Balsiger, H., Geiss, J., Goldstein, R., Ip, W.-H., Meier, A., Neugebauer, M., Rosenbauer, H., and Shelley, E.: 1993, 'The Ion Population between 1,300 km and 230,000 km in the Coma of Comet P/Halley', *Astron. Astrophys.* **279**, 260.

Altwegg, K., Balsiger, H., and Geiss, J.: 1994, 'Abundance and Origin of the CH_n^+ Ions in the Coma of Comet Halley', *Astron. Astrophys.* **290**, 318.

Anderson, C. M.: 1997, 'Fiberoptically Multiplexed Medium Resolution Spectroscopy from the WIYN Telescope, Singlet D Neutral Oxygen NH_2, and H_2O', *Earth, Moon, and Planets* **78**, 99–104.

Balsiger, H., Altwegg, K., Bühler, F., Geiss, J., Ghielmetti, A. G., Goldstein, B. E., Goldstein, R., Huntress, W. T., Ip, W.-H., Lazarus, A. J., Meier, A., Neugebauer, M., Rettenmund, U., Rosenbauer, H., Schwenn, R., Sharp, R. D., Shelley, E. G., Ungstrup, E., and Young, D. T.: 1986, 'Ion Composition and Dynamics at Comet Halley', *Nature* **321**, 330.

Biver, N., Bockelee-Morvan, D., Colom, P. Crovisier, J., Davies, J., Dent, W., Despois, D., Gerard, E., Lellouch, E., Rauer, H., Moreno, R., and Paubert, G.: 1997, *Science* **275**, 1915.

Brio, M. and Wu, C. C.: 1988, 'An Upwind Differencing Scheme for the Equations of Ideal Magnetohydrodynamics', *J. Comput. Phys.* **75**, 400.

Coates, A. J., Johnstone, A. D., Wilken, B., Jockers, K., and Glassmeier, K. H.: 1989, 'Velocity-Space Diffusion of Pickup Ions from Water Group at Comet Halley', *J. Geophys. Res.* **94**, 9983.

Coates, A. J., Johnstone, A. D., Wilken, B., and Neubauer, F.: 1993, 'Velocity Space Diffusion and Nongyrotropy of Pickup Water Group Ions at Comet Grigg-Skjellerup', *J. Geophys. Res.* **98**, 20.

Cravens, T. E.: 1986, 'The Physics of the Cometary Contact Surface', in B. E. Battrick, E. J. Role, and R. Reinhard (eds.), *Proc. of 20th ESLAB Symposium on the Exploration of Halley's Comet*, ESA SP-250, **1**, 241.

Cravens, T. E.: 1989, 'A Magnetohydrodynamical Model of the Inner Coma of Comet Halley', *J. Geophys. Res.* **94**, 15,025.

Cravens, T. E.: 1990, 'Collisional Processes in Cometary Plasmas', in A. J. Coates and A. D. Johnstone (eds.), *Cometary Plasma Processes*, AGU, Washington, D.C.

Cravens, T. E.: 1997, 'Comet Hyakutake X-ray Source: Charge Transfer of Solar Wind Heavy Ions', *Geophys. Res. Lett.* **24**, 105.

Damas, M. C. and Mendis, D. A.: 1992, '3D Axisymmetric Photo-Chemical Flow Model of the Cometary Inner Shock Layer', *Astrophys. J.* **396**, 704.

Dennerl, K., Englhauser, J., and Trümper, J: 1997, 'X-Ray Emissions from Comets Detected in the Röntgen X-ray Satellite All-Sky Survey', *Science* **277**, 1625.

DeZeeuw, D. and Powell, K. G.: 1992, 'An Adaptively-Refined Cartesian Mesh Solver for the Euler Equations', *J. Comput. Phys.* **104**, 55.

Eberhardt, P. and Krankowsky, D.: 1995, 'The Electron Temperature in the Inner Coma of Comet P/Halley', *Astron. Astrophys.* **295**, 795.

Festou, M. C., Rickman, H., and West, R. M.: 1993a, 'Comets, I. Concepts and Observations', *Astron. and Astrophys. Rev.* **4**, 363.

Festou, M. C., Rickman, H., and West, R. M.: 1993b, 'Comets, II. Models, Evolution, Origin and Outlook', *Astron. and Astrophys. Rev.* **5**, 37.

Fitzsimmons, A. and Cartwright, M.: 1996, *MNRAS*, **278**, L37.

Goldstein, B. E., Altwegg, K., Balsiger, H., Fuselier, S. A., Ip, W.-H., Meier, A., Neugebauer, M., Rosenbauer, H., and Schwenn, R.: 1989, 'Observations of a Shock and a Recombination Layer at the Contact Surface of Comet Halley', *J. Geophys. Res.* **94**, 17,251.

Gombosi, T. I.: 1987, 'Charge Exchange Avalanche at the Cometopause', *Geophys. Res. Lett.* **14**, 1174.

Gombosi, T. I.: 1988, 'Preshock Region Acceleration of Implanted Cometary H^+ and O^+', *J. Geophys. Res.* **93**, 35.

Gombosi, T. I.: 1991, 'The Plasma Environment of Comets', *Rev. Geophys.* **29**, 976.

Gombosi, T. I. (ed.): 1993, 'Plasma Environments of Non-Magnetic Planets', Pergamon Press, Oxford.

Gombosi, T. I.: 1994, 'Gaskinetic Theory', Cambridge University Press, Cambridge.

Gombosi, T. I., Nagy, A. F., and Cravens, T. E.: 1986, 'Dust and Neutral Gas Modeling of the Inner Atmospheres of Comets', *Rev. of Geophys.* **24**, 667.

Gombosi, T. I., Neugebauer, M., Johnstone, A. D., Coates, A. J., and Huddleston, D. E.: 1991, 'Comparison of Observed and Calculated Implanted Ion Distributions Outside Comet Halley's Bow Shock', *J. Geophys. Res.* **96**, 9467.

Gombosi, T. I., Powell, K. G., and DeZeeuw, D. L.: 1994, 'Axisymmetric Modeling of Cometary Mass Loading on an Adaptively Refined Grid: MHD Results', *J. Geophys. Res.* **99**, 21,525.

Gombosi, T. I., De Zeeuw, D. L., Häberli, R., and Powell, K. G.: 1996, 'A 3D Multiscale MHD Model of Cometary Plasma Environments', *J. Geophys. Res.* **101**, 15,233.

Gosling, J. T.: 1998, 'The Solar Wind', in P. Weissman, L-A. McFadden, and T. Johnson (eds.), *Encyclopedia of the Solar System*, Academic Press, London.

Gringauz, K. I. and Verigin, M. I.: 1991, 'Permanent and Nonstationary Plasma Phenomena in Comet Halley's Head', in A. D. Johnstone (ed.), *Cometary Plasma Processes*, AGU, Washington, D.C., p. 107.

Gringauz, K. I., Gombosi, T. I., Tátrallyay, M., Verigin, M. I., Remizov, A. P., Richter, A. K., Apáthy, I., Szemerey, I., Dyachkov, A. V., Balakina, O. V., and Nagy, A. F.: 1986, 'VEGA Observations of the Cometopause and Cometary Plasma Region', *Geophys. Res. Lett.* **13**, 613.

Häberli, R. M., Combi, M. R., Gombosi, T. I., DeZeeuw, D. L., and Powell, K. G: 1997a, 'Quantitative Analysis of H_2O^+ Coma Images', *Icarus* **130**, 373.

Häberli, R. M., Gombosi, T. I., Combi, M. R., DeZeeuw, D. L., and Powell, K. G: 1997b, 'Modeling of Cometary X-Rays Caused by Solar Wind Minor Ions', *Science* **276**, 939.

Huebner, W. F. (ed.): 1990, *Physics and Chemistry of Comets*, Springer-Verlag, Berlin.

Hynds, R. J., Cowley, S. W. H., Sanderson, T. R., Wenzel, K.-P., and Van Rooijen, J. J.: 1986, 'Observations of Energetic Ions from Comet Giacobini-Zinner', *Science* **232**, 361.

Ip, W.-H. and Axford, W. I.: 1990, 'The Plasma', in W. F. Huebner (ed.), *Physics and Chemistry of Comets*, Springer-Verlag, Berlin, p. 177.

Ip, W.-H., Schwenn, R., Rosenbauer, H., Balsiger, H., Neugebauer, M., and Shelley, E. G.: 1987, 'An Interpretation of the Ion Pile-Up Region Outside the Ionospheric Contact Surface', *Astron. Astrophys.* **187**, 132.

Jewett, D., Senay, M., and Matthews, H.: 1996, *Science* **271**, 1110.

Jockers, K., Credner, T., Karpov, N., and Sergeev, A.: 1996, *IAU Circular*, No. 6468.

Körösmezey, A., Cravens, T. E., Gombosi, T. I., Nagy, A. F., Mendis, D. A., Szegö, K., Gribov, B. E., Sagdeev, R. Z., Shapiro, V. D., and Shevchenko, V. I.: 1987, 'A Comprehensive Model of Cometary Ionospheres', *J. Geophys. Res.* **92**, 7331.

Lisse, C. M., Dennerl, K., Englhauser, J., Harden, M., Marshall, F. E., Mumma, M. J., Petre, R., Pye, J. P., Ricketts, M. J., Schmitt, J., Trümper, J., and West, R. G.: 1996, 'Discovery of X-Ray and Extreme Ultraviolet Emission from Comet C/Hyakutake 1996 B2', *Science* **274**, 205.

McKenna-Lawlor, S., Kirsch, E., O'Sullivan, D., Thompson, A., and Wenzel, K.-P.: 1986, 'Energetic Ions in the Environment of Comet Halley', *Nature* **321**, 347.

Mendis, D. A., Houpis, H. L. F., and Marconi, M. L.: 1985, 'The Physics of Comets', *Fund. Cosmic Phys.* **10**, 1.

Motschmann, U., and Glassmeier, K.-H.: 1993, 'Nongyrotropic Distribution of Pickup Ions at Comet P/Grigg-Skjellerup: A Possible Source of Wave Activity', *J. Geophys. Res.* **98**, 20.

Mumma, M. J., Krasnopolsky, V. A., and Arbott, M. J.: 1997, 'Soft X-Rays from Four Comets Observed with EUVE', *Astrophys. J.* **491**, L125.

Nagai, T., Waite, J. H., Green, J. L., Chappell, C. R., Olsen, R. C., and Comfort, R. H.: 1984, 'First Measurements of Supersonic Polar Wind in the Polar Magnetosphere', *Geophys. Res. Lett.* **11**, 669.

Neubauer, F. M.: 1988, 'The Ionopause Transition and Boundary Layers at Comet Halley from Giotto Magnetic Field Observations', *J. Geophys. Res.* **93**, 7272.

Neubauer, F. M., Glassmeier, K. H., Pohl, M., Raeder, J., Acuna, M. H., Burlaga, L. F., Ness, N. F., Musmann, G., Mariani, F., Wallis, M. K., Ungstrup, E., and Schmidt, H. U.: 1986, 'First Results from the Giotto Magnetometer Experiment at Comet Halley', *Nature* **321**, 352.

Neugebauer, M.: 1990, 'Spacecraft Observations of the Interaction of Active Comets with the Solar Wind', *Rev. Geophys.* **28**, 231.

Neugebauer, M., Lazarus, A. J., Balsiger, H., Neubauer, F. M., Schwenn, R., and Shalley, E. G.: 1989, 'The Velocity Distribution of Cometary Protons Picked up by the Solar Wind', *J. Geophys. Res.* **94**, 5227.

Newburn, R. L., Neugebauer, M., and Rahe, J. (eds.): 1991, *Comets in the Post-Halley Era*, Kluwer Academic Publishers.

Powell, K. G.: 1994, 'An Approximate Riemann Solver for Magnetohydrodynamics (That Works in More Than One Dimension)', *ICASE Report* No. 94-24, Langley, VA.

Powell, K. G., Roe, P. L., Myong, R. S., Gombosi, T. I., and DeZeeuw, D. L.: 1995, 'An Upwind Scheme for Magnetohydrodynamics', in *Proceedings of AIAA 12th Computational Fluid Dynamics Conference*, AIAA, San Diego, p. 661.

Powell, K. G., De Zeeuw, D. L., Gombosi, T. I., and Roe, P. L.: 1999, 'Multiscale Adaptive Upwind Scheme for Magnetohydrodynamics: MAUS-MHD', *J. Comput. Phys.* **154**, 284.

Rauer, H., Arpigny, C., Boehnhardt, H., Colas, F., Crovisier, J., Jorda, L., Kuppers, M., Manfroid, J., Rembor, K., and Thomas, N.: 1997, *Science* **275**, 1909.

Réme, H.: 1991, 'Cometary Plasma Observations between the Shock and the Contact Surface', in A. D. Johnstone (ed.), *Cometary Plasma Processes*, AGU, Washington, D.C., p. 87.

Schleicher, D. G., Lederer, S. M., Millis, R. L., and Farnham, T. L.: 1997, *Science* **275**, 1913.

Somogyi, A. J., Gringauz, K. I., Szegö, K., Szabó, L., Kozma, G., Remizov, A. P., Erö, J., Jr., Klimenko, I. N., Szücs, I. T., Verigin, M. I., Windberg, J., Cravens, T. E., Dyachkov, A., Erdös, G., Faragó, M., Gombosi, T. I., Kecskeméty, K., Keppler, E., Kovács, T., Jr., Kondor, A., Logachev, Y. I., Lohonyai, L., Marsden, R., Redl, R., Richter, A. K., Stolpovskii, V. G., Szabó, J., Szentpétery,

I., Szepesváry, A., Tátrallyay, M., Varga, A., Vladimirova, G. A., Wenzel, K.-P., and Zarándy, A.: 1986, 'First Observations of Energetic Particles Near Comet Halley', *Nature* **321**, 285.

Tanaka, T.: 1993, 'Configurations of the Solar Wind Flow and Magnetic Field around the Planets with no Magnetic Field: Calculation by a New MHD Simulation Scheme', *J. Geophys. Res.* **98**, 17,251.

van Leer, B.: 1979, 'Towards the Ultimate Conservative Difference Scheme, V. A Second-Order Sequel to Godunov's Method', *J. Comput. Phys.* **101**.

van Leer, B., Tai, C. H., and Powell, K. G.: 1989, 'Design of Optimally-Smoothing Multi-Stage Schemes for the Euler Equations', in *Proceedings of AIAA 9th Computational Fluid Dynamics Conference*, AIAA-89-1933-CP, AIAA, Washington, D.C..

Wagner, R. M. and Schleicher, D. G.: 1997, *Science* **275**, 1918.

Wallis, M. K. and Dryer, M.: 1976, 'Sun and Comets as Sources in an External Flow', *Astrophys. J.* **205**, 895.

Weaver, H. A., Feldman, P. D., A'Hearn, M. F., Arpigny, C., Brandt, J. C., Festou, M. C., Haken, M., McPhate, J. B., Stern, S. A., and Tozzi, G. P.: 1997, *Science* **275**, 1900.

Whipple, F. L.: 1950, 'The Acceleration of Comet Encke', *Astrophys. J.* **111**, 375.

Zachary, A. and Colella, P.: 1992, 'A Higher-Order Godunov Method for the Equations of Ideal Magnetohydrodynamics', *J. Comput. Phys.* **99**, 341.